Numerical investigation of the flow through fold-cores with LSDyna ICFD Solver

Fabian Muhs[1], Ralf Walter[1]

[1]Institute of Aircraft Design, University of Stuttgart

1 Abstract

In this work, the flow behavior of sandwich foldcores and their influence on the fluidic parameters such as pressure drop are investigated. The subjects of the investigation are three different foldcore geometries, which are analyzed with the ICFD solver from LSDyna. The results are then examined with results from numerical simulations using OpenFoam as well as experiments in the water channel.

2 Introduction

Foldcores represent a promising alternative to conventional sandwich core structures such as honeycombs or foams. The manufacturing process follows the principle of origami - folding edges are applied to a flat semi-finished product and then a three-dimensional core structure is created by folding the semi-finished product, as shown in Fig. 1. Suitable materials for producing these foldcores are cellular and technical papers, plastics, metals or fiber composites. [1,2]

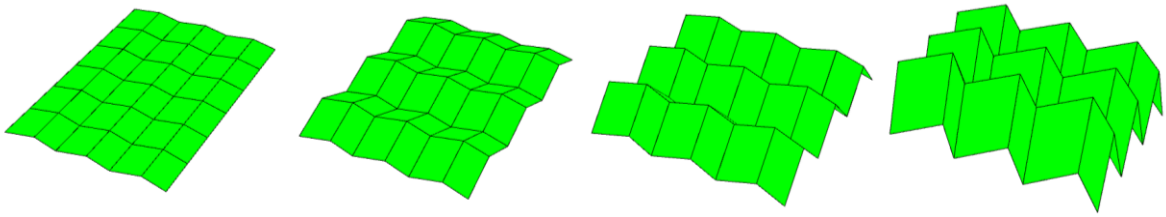

Fig.1: Principle of foldcores illustrated on a 3x3 Miura-ori foldcore.

An infinite variety of different geometric designs can be realized by the folding process. A decisive advantage over the honeycombs and foams frequently used in industry is the possibility of creating an open core structure as shown in Fig. 2. On the one hand, this enables a drainage function to avoid moisture accumulation in the sandwich core and the associated reduction in mechanical properties. On the other hand, these channels in the core structure can also be actively used for media transport and associated cooling or heating. This aspect of functional integration will be investigated in more detail in this work.

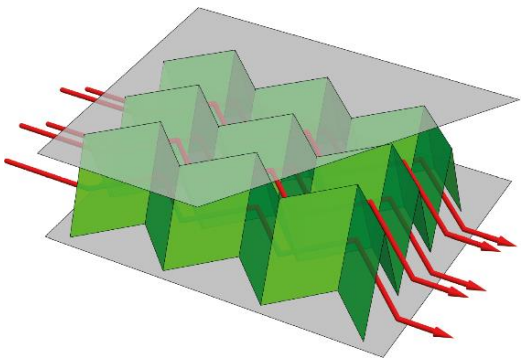

Fig.2: Miura-ori foldcore structure with open core geometry shown by the red arrows.

3 Theory of flow in curved channels

In the present work, flow in curved, non-circular channels are considered. In these, phenomena occur which not only influence the physical quantities such as the pressure drop but can also lead to numerical instabilities. In particular, the occurrence of flow separation and secondary flows are to be mentioned here.

3.1 Flow separation and secondary flows

In technical flows with directional changes, as they occur in pipe or channel flows at hand here, flow separation areas often form. This phenomenon can be divided into two main effects. These are shown in Fig. 3 and marked with the letters A and B.

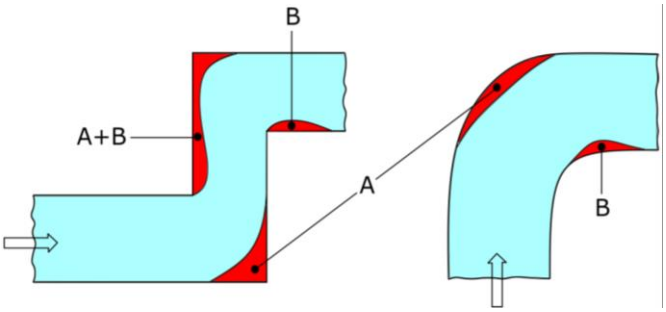

Fig.3: Flow separation areas (red) in curved channels. A: Flow separation due to the increasing pressure in the direction of the outer radius. B: Flow separation due to effective cross-sectional expansion. Figure adapted from [3].

In the flow region A, the fluid particles are on a circular path with radius r and normal direction n. It is to be assumed that neither frictional nor gravitational forces act on the fluid particles. In this case there is equilibrium of forces between pressure force and centrifugal force and according to Newton's second law applies with the pressure p, the density ρ and the velocity of the fluid particle u_i:

$$\frac{\partial p}{\partial n} = \rho \frac{u_i^2}{r} \tag{1}$$

Formula (1) shows that the pressure increases as the radius r increases. In the wall area, the fluid particles are slowed down due to friction. As a result, the fluid particles can no longer overcome the increased pressure and a flow separation occurs, accompanied by a backflow and vortex formation. The area A of the flow separation is also called backwater area and causes an effective narrowing of the flow cross section, which results in an increase of the flow velocity due to the continuity condition.
The flow detachment area B is formed as a direct consequence of the detachment in area A. Due to an effective widening of the flow cross-section after the bend, there is a decrease in the flow velocity and an increase in the static pressure. The fluid particles located on the inner wall are slowed down by friction and cannot overcome the pressure increase. A second flow separation occurs.

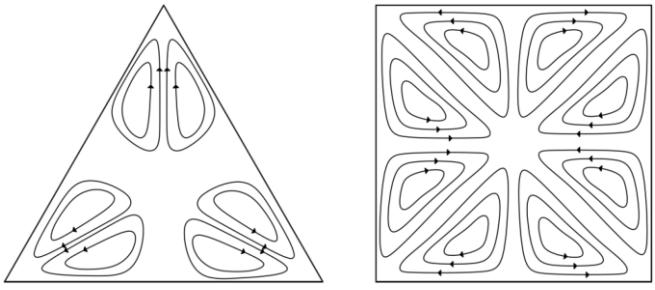

Fig.4: Representation of secondary flow of second type for turbulent flow through non-circular cross-sections according to [4].

Another flow phenomenon is the occurrence of secondary flows in the channel. The reduction in velocity of the fluid particles near the wall due to friction causes a disturbance of the equilibrium between pressure and centrifugal force in equation (1). As a result, superimposed on the main flow, circulatory motions of the fluid particles are formed in the cross-sectional plane, which are called secondary flow and are shown in Fig. 4 for a triangular and square cross-section. The explicit generation and formation of such secondary flow forms is the subject of current research, since the occurrence of turbulence complicates the theoretical consideration (for laminar flows, such effects could not be observed so far). Detailed theoretical investigations can be found in [5], among others.

3.2 Pressure loss

An essential parameter when considering duct flows is the pressure drop Δp_v. This results directly from the energy loss due to heat (dissipation losses), which is caused by the friction of the fluid on the channel walls. The theoretical static pressure p is consequently reduced by the pressure loss Δp_v. This in turn depends on a variety of factors such as pipe friction, flow inlet, deflections and changes in cross-section. The theoretical description of the pressure loss is only possible for very simple special cases with laminar flow. In practice, the pressure loss is often modeled as the product of the drag coefficient ζ and the dynamic pressure:

$$\Delta p_v = \zeta \, \rho \frac{u^2}{2} \tag{1}$$

Due to the variety of different duct shapes, branching or deflection internals and flow phenomena, the resistance coefficient can only be obtained from tests in practice. It is usually composed of a friction component ζ_R and a geometric component ζ_G. For low Reynold numbers ($Re < 4x10^4$), a hydraulically smooth channel can be assumed according to [6] and the dependence of the drag coefficient on the wall roughness does not apply.

4 Modell Setup

4.1 Considered foldcore geometries

To cover the wide range of possible foldcore geometries, three representative configurations were selected in this work. Since the sandwich foldcore is bonded to the top and bottom face sheets, the individual channels can be viewed independently as shown in Fig. 5. This significantly reduces the numerical effort and modeling.

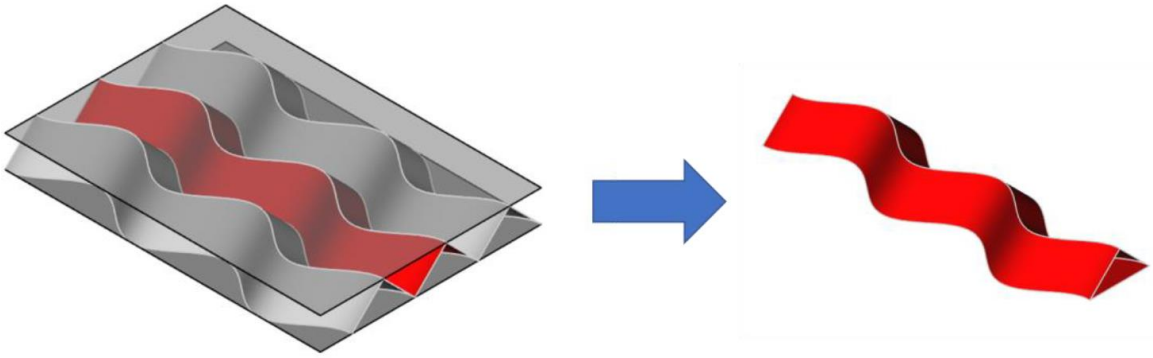

Fig.5: Independent observation of a single channel with a sinusoidal shape [7].

The three selected foldcore geometries represent typical configurations and match the geometries from [8] to be able to compare the numerical results. The first channel K1 has a rectangular cross-section and is shown in Fig. 6. The course is sinusoidal. At the inlet and outlet, a linear piece of 30mm length was added to improve the convergence behavior of the simulation and to provide a run-up distance for the turbulent flow. This procedure was also carried out for the channels K2 and K3. Channel K2 also has a sinusoidal shape, but compared to K1 it has a triangular cross-section as shown in Fig. 6. A triangular cross-section was also selected for channel K3. The course is described by linear functions resulting in a zigzag pattern as shown in Fig. 6. Comparing the geometries, it can be seen that channel K2 is an blended geometry of K1 and K3 - the sinusoidal shape of K1 and the cross section adapted from K3. This should simplify the comparison of the channels with each other as well as the identification of geometry-related flow effects.

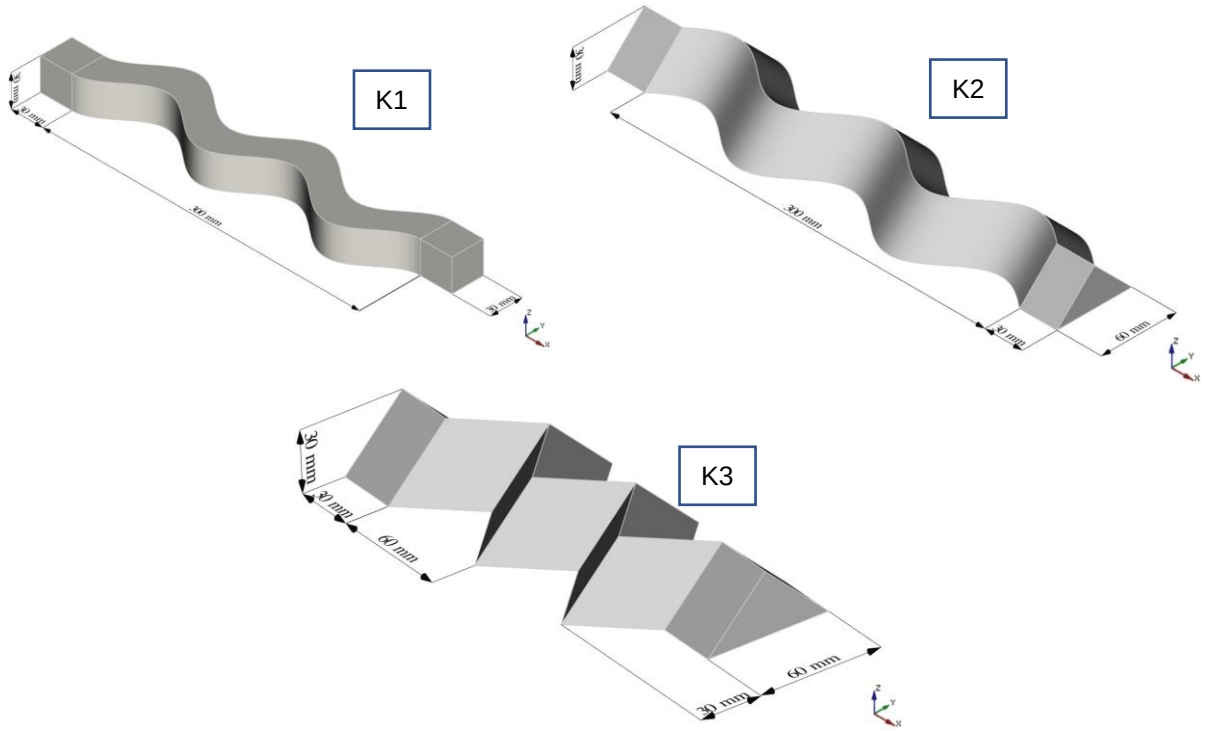

Fig.6: Considered channel geometries K1 to K3 with characteristic dimensions [7].

4.2 Mesh generation

When creating the mesh, special attention must be paid to the mesh quality and resolution in the areas close to the wall. In the used version R12 of LSDyna ICFD only High-Re models are implemented, which provide a total of four different wall functions. All these wall functions have a switchover point from the logarithmic to the linear, dimensionless velocity curve at 11,225 units of the dimensionless wall distance y^+. This is to ensure that there are no large deviations from the true, near-wall velocity profile. If an element node is below this switchover point, the wall function switches to the linear course.
However, due to the flow phenomena described in section 3 for the foldcore geometries considered here, this procedure leads to very strong convergence problems and implausible results. In addition, relatively low Reynolds numbers result in a large boundary layer thickness. The boundary layer thickness δ is inversely proportional to the square root of the Re number. These circumstances lead to the fact that the y^+-values of the element nodes near the wall are below the optimal range $30 < y^+ < 300$ given in the literature [9]. This problem is illustrated in Fig. 7 for channel K1.

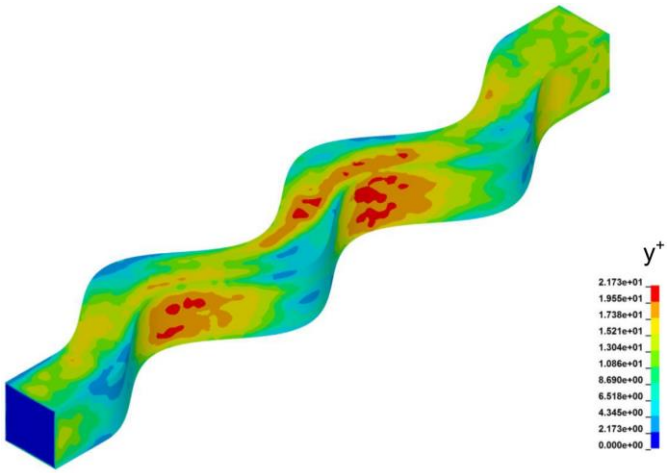

Fig.7: Visualization of the y^+-values on the side walls of the channel geometry K1 [7].

To eliminate the described problem of frequent switching of the wall function, LSDyna ICFD offers the possibility of boundary layer refinement. The elements close to the wall are divided into two or more smaller elements. This methodology is intended to ensure that all element nodes are in the linear region of the turbulent boundary layer. In application, this approach could not lead to the desired result for the geometries and boundary conditions present here. The numerical simulations diverged after a short time. Comparative calculations with pipe flows and similar boundary conditions showed good results. This allows the conclusion that the non-circular cross-sections and the associated flow phenomena are the cause of the problem. For this reason, an alternative meshing methodology had to be found.
The meshing methodology used in this work is based on the idea of using a coarser volume mesh in the near-wall region and a fine volume mesh in the core flow region. In this way, it can be ensured that the y^+-values of the nodal points are shifted upwards and the simulation thus remains stable. At the same time, the fine volume mesh of the core flow ensures plausible results, which can be compared with [8]. The procedure for this meshing is shown in Fig. 8 using the example of channel K1.

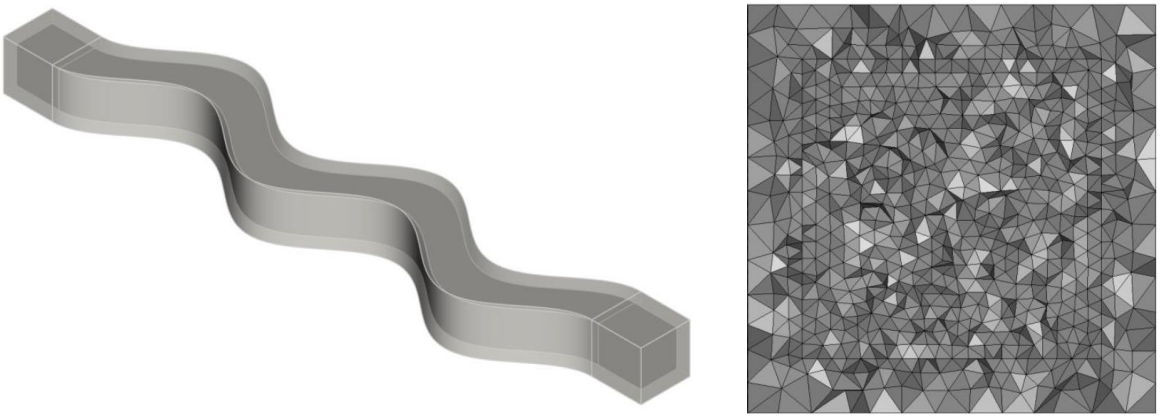

Fig.8: Left: Channel geometry K1 with two closed surfaces lying inside each other to create the mesh. Right: Cross-section of channel K1 with generated mesh.

The automatic volume mesher in LSDyna is used to create the mesh. The resulting mesh is shown in Fig. 8 on the right side in the cross section of channel K1. The use of this meshing results in significantly improved convergence behavior as well as plausible results for the pressure drop and pressure forces on the side walls of the duct.
A disadvantage of the presented methodology, besides the increased effort for mesh generation, is the fact that no frictional forces on the wall can be output. Refinement of the boundary layer would be necessary to output these values, which will result in the above described problems.

As part of this work, a mesh convergence study was conducted according to [10]. Thereby, the interior mesh of the core flow was refined three times. The effective convergence order was determined to be $p_{con} = 1.4$ and is below the theoretical convergence order of $p_{con,theo} = 2$. This is due to the turbulence model, the wall functions as well as the mesh quality.
An edge length of $h_{in} = 1.25\ mm$ could be determined as the optimal element size. This represents the best compromise between accuracy and simulation time (<2h @ 32 CPUs).

4.3 Boundary conditions

For the boundary conditions, analogous to the works [11] and [8], water was used as the flow medium with an inlet velocity of $U_\infty = 0.14 \frac{m}{s}$. The outlet pressure was chosen to be $p_0 = 0\ Pa$, so that the difference between inlet and outlet pressure, which represents the pressure loss Δp_v, corresponds to the inlet pressure. In order to specify the adhesion condition to the side walls of the channels, the flow velocity was chosen here to be $U_{Wall} = 0 \frac{m}{s}$. The boundary conditions described are identical for all three geometries presented.
The modeling of the turbulence boundary conditions differs due to the different cross sections for each geometry. The turbulent kinetic energy results from the definition equation of the degree of turbulence to:

$$k = \frac{3}{2}(Tu\ U_\infty)^2 \tag{2}$$

For flow problems, $Tu = 0.05$ is often assumed for the turbulence level at the inlet. This also corresponds to the default value in LSDyna ICFD. For the dissipation rate ε, the following relationship can be assumed according to Prandtl [12]:

$$\varepsilon = 0.16 \frac{k^{1.5}}{\tilde{L}} \tag{3}$$

Here $\tilde{L}$ corresponds to the length of the large turbulence bales, for which the assumption $\tilde{L} = 0.1\ D_h$ can be made based on empirical values. The hydraulic diameter D_h is $D_h = 30\ mm$ for channel K1 and $D_h = 24.8\ mm$ for channels K2 and K3 respectively. For non-circular cross-sections, the hydraulic diameter is derived according to [3] as is $D_h = 4\ \frac{A}{U}$. Here, A denotes the cross-section and U the wetted circumference.
When using k-ω- or SST-turbulence models, the specific dissipation rate ω at the inlet must also be specified. In the present work, the following definition equation is used [9]:

$$\omega = \frac{\varepsilon}{k} \tag{4}$$

The turbulence boundary conditions presented apply when using k-ε-, k-ω-, and SST turbulence models. For the flow problems considered in this work, only the SST model has proven to be suitable. The other turbulence models as well as the alternative "Variational Multiscale Approach" led to divergence and implausible results. The following Table 1 summarizes the boundary conditions in tabular form.

Table 1: Boundary conditions of channels K1 to K3.

Geometry	$k * 10^5[\frac{m^2}{s^2}]$	$\varepsilon * 10^5[\frac{m^2}{s^3}]$	$\omega\ [\frac{1}{s}]$	$U_\infty\ [\frac{m}{s}]$	$p_0\ [Pa]$	$U_{Wall}\ [\frac{m}{s}]$
K1	7.35	3.36	0.457	0.14	0	0
K2 & K3	7.35	4.05	0.551	0.14	0	0

5 Results

To evaluate the convergence behavior of the simulations, the residual is evaluated on the one hand. This should have a magnitude of 10^{-5} to 10^{-6} in order to obtain high-quality results. On the other hand, the integral quantities pressure loss Δp_v and the pressure force F_{py} on the channel wall are considered. If the integral values are constant, the simulation can be considered as converged, even if the residual has not yet reached the required magnitude. In addition to these characteristic values, the fluidic phenomena such as vortex formation, flow separation and backflow are visualized and compared on the basis of the results using OpenFoam [8] and the experimental data [11]. For the visualization the "Line integral Convolution" (LIC) method as well as for the representation of the vortices the Q-criterion [13] are used.

To improve the convergence behavior of the simulations, the under-relaxation method is used. This represents an artificial numerical damping, which is implemented in the iteration process. After each iteration step, a flow quantity f_{new} then corresponds to a linear combination of the current $f_{current}$ and the value f_{old} calculated in the previous iteration step. Equation 5 illustrates this using the example of the flow variable pressure p:

$$p_{new} = \alpha\ p_{current} + (1 - \alpha)\ p_{old} \tag{5}$$

In this context, the parameter α represents an under-relaxation parameter and should lie in the interval $(0,1]$. In the simulations carried out within the scope of this work, the under-relaxation parameter was

set to $\alpha = 0.6$. It should be noted that this strongly decreases the convergence rate. Thus, significantly more iterations are necessary to achieve convergence.

The results of the numerical flow simulation for channels K1 to K3 are shown in Fig. 9 to Fig. 11. On the left side, the course of the residuals for the impulse and the pressure over the number of iterations is shown. On the right side, the course of the integral quantities over the number of iterations is shown. The results of the simulations as well as the comparative values of the OpenFoam simulations according to [8] are shown in Table 2
The results of the integral quantities for channel K1 show a deviation of about 46% for the pressure drop and about 58% for the pressure force. These relatively large deviations are due to the cross-sectional shape of the channel and the associated secondary flows. During the simulation, poorer convergence behavior was already evident compared to cores K2 and K3.
Since the channel geometry of K1 has a sinusoidal shape and a square cross-section, there is very little vortex formation and flow separation. Therefore, channel K1 has the lowest pressure drop.

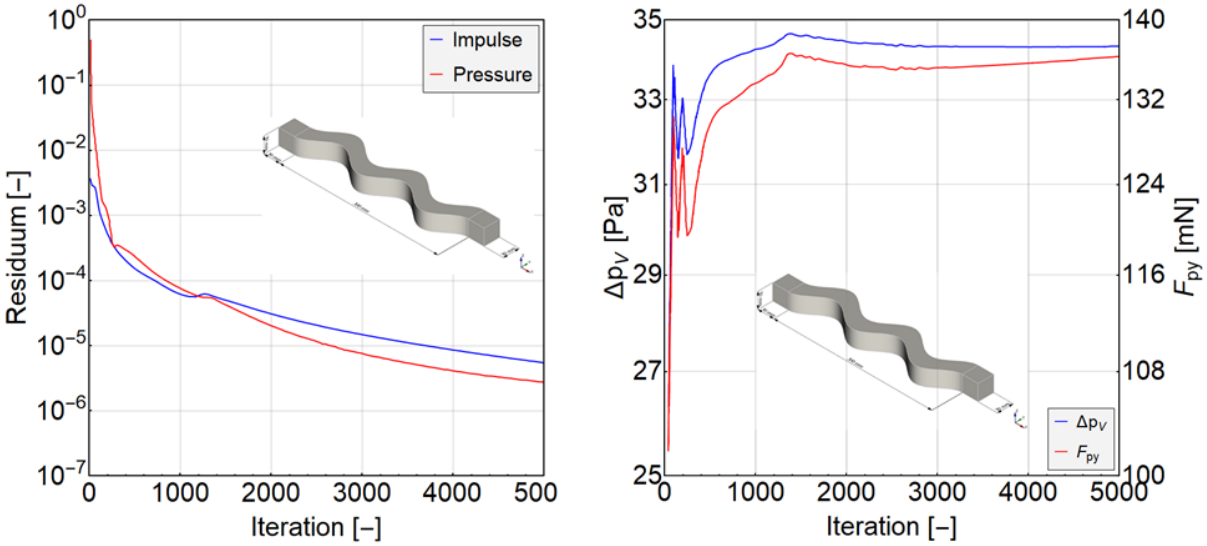

Fig.9: Left: Plot of residuals versus the number of iterations for the pulse and pressure of channel K1. Right: Course of the integral quantities pressure loss Δp_V and pressure force F_{py} over the number of iterations of channel K1.

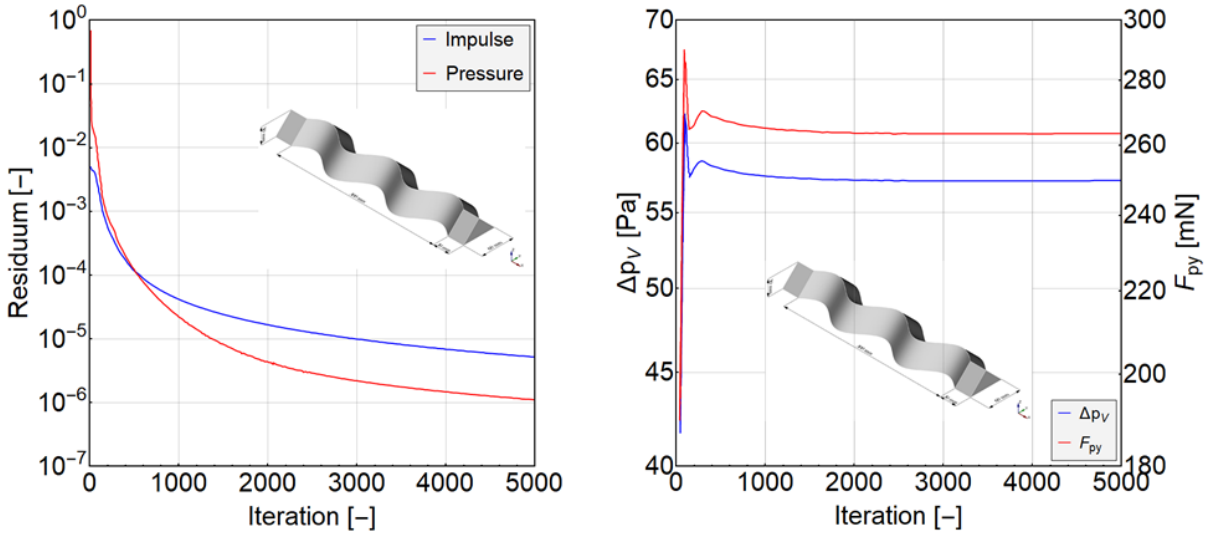

Fig.10: Left: Plot of residuals versus the number of iterations for the pulse and pressure of channel K2. Right: Course of the integral quantities pressure loss Δp_V and pressure force F_{py} over the number of iterations of channel K2.

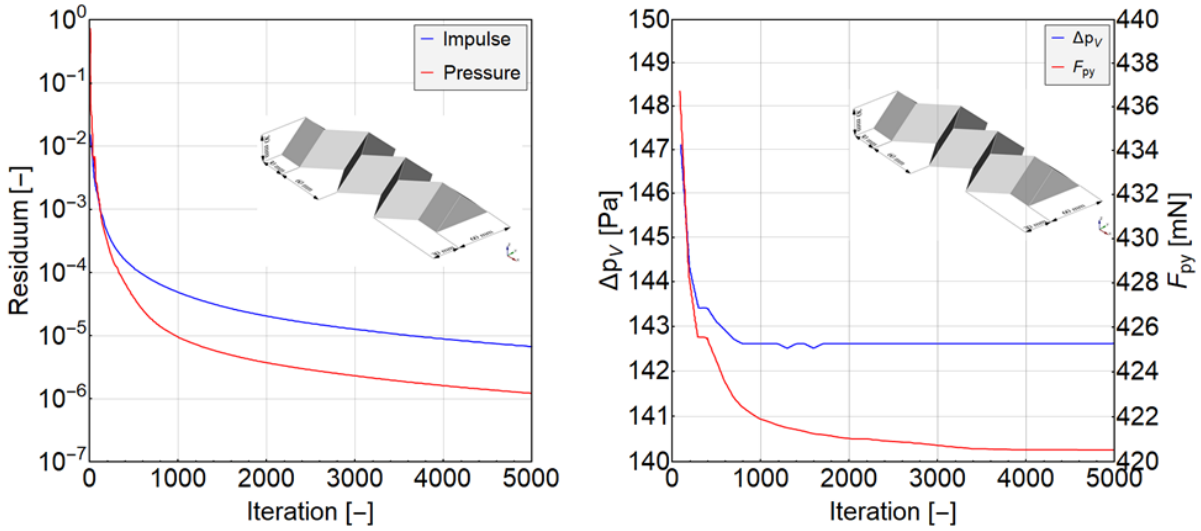

Fig.11: Left: Plot of residuals versus the number of iterations for the pulse and pressure of channel K3. Right: Course of the integral quantities pressure loss Δp_V and pressure force F_{py} over the number of iterations of channel K3.

Table 2: Results of the integral quantities of the numerical simulation as well as comparative values of the calculations performed with OpenFoam according to [8].

Geometry	Value	Result	Comparative value [8]
K1	Pressure loss Δp_v [Pa]	34.3	23.38
	Pressure force F_{py} [mN]	133.3	84.1
K2	Pressure loss Δp_v [Pa]	57.2	57.7
	Pressure force F_{py} [mN]	263.5	276.6
K3	Pressure loss Δp_v [Pa]	142.6	172.3
	Pressure force F_{py} [mN]	420.5	540.3

For channel geometry K2, there is very good agreement between the results of this work and those obtained with OpenFoam in Table 2. The deviation for the pressure drop is negligible, and the deviation for the compressive force is below 5%. In order to check whether the essential flow phenomena are represented, the vortex formation of the two numerical results and the experimental data in the water channel were compared in Fig. 12. There is a very good agreement between all methods.

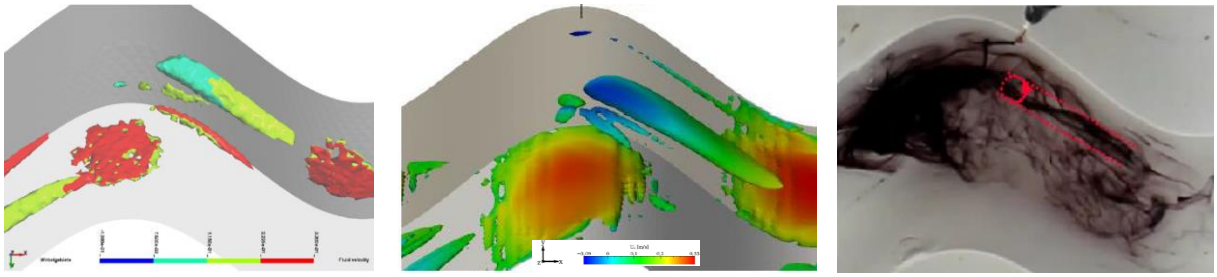

Fig.12: Left: Vortex regions of numerical simulation. Middle: Vortex regions of the OpenFoam simulations according to [8]. Right: Experimental results according to [11].

The visualization of the flow separation by the LIC method in Fig. 13 also shows a very good agreement between the numerical methods and the experimental data. Due to the transverse pressure equation, a higher static pressure prevails in the area close to the wall than in the center of the channel. As a result, the flow detaches here first. This wake water region after the crest of the sinusoidal edge, which is caused by the detachment, can be mapped by all three methods.

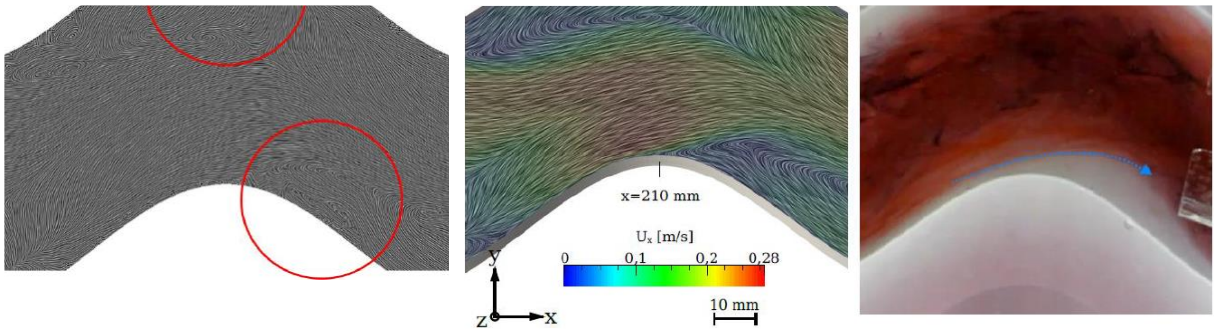

Fig.13: Illustration of flow separation in channel K2 using LIC method. Left: Numerical results of this work. Center: Results of the OpenFoam simulations [8]. Right: Experimental results of the water channel [11].

For channel K3, there is a good agreement between the simulations with LSDyna ICFD and the OpenFoam resultet, shown in Table 2. The deviation for the pressure drop is 17%, for the compressive force the deviation is 22%. Comparing the visualization of the vortex regions in Fig. 14 and the flow separation in Fig. 15, good agreements are shown for all three methods. The flow is characterized by a narrow core flow with large wake water regions at the edges.

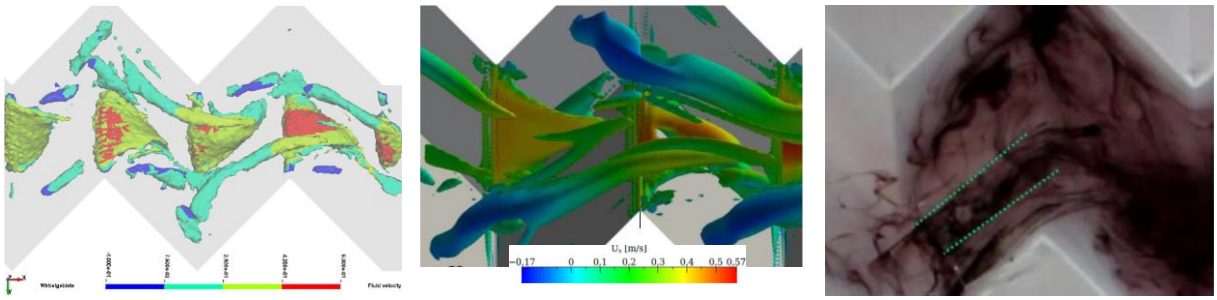

Fig.14: Left: Vortex regions of numerical simulation. Middle: Vortex regions of the OpenFoam simulations according to [8]. Right: Experimental results according to [11].

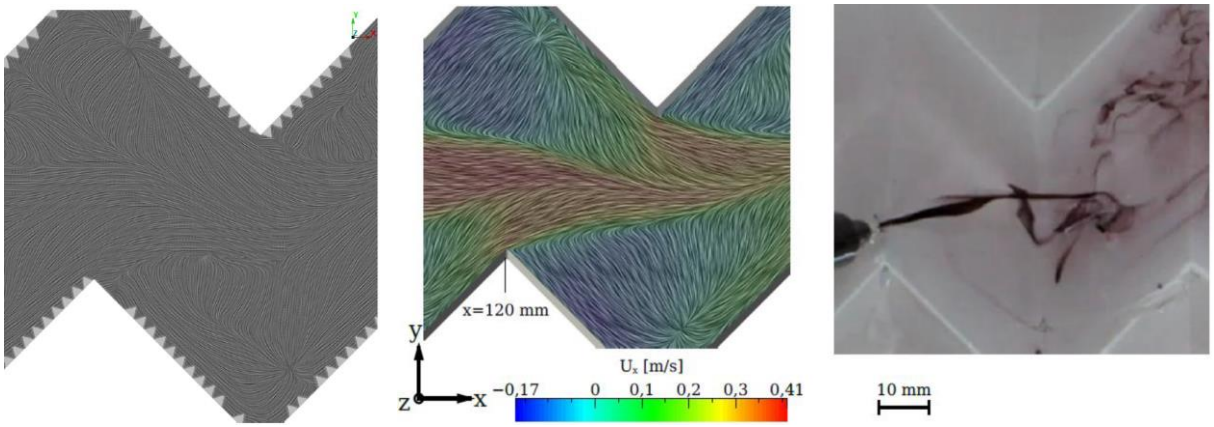

Fig.15: Illustration of flow separation in channel K3 using LIC method. Left: Numerical results of this work. Center: Results of the OpenFoam simulations [8]. Right: Experimental results of the water channel [11].

As expected, the highest pressure losses occur in channel K3. This is due to the large-volume wake water areas with strong vortex formation, which extract a lot of energy from the flow. The cause of these wake water areas lies in the zigzack course of the foldcore geometry. This is illustrated by the streamlines in Fig. 16.

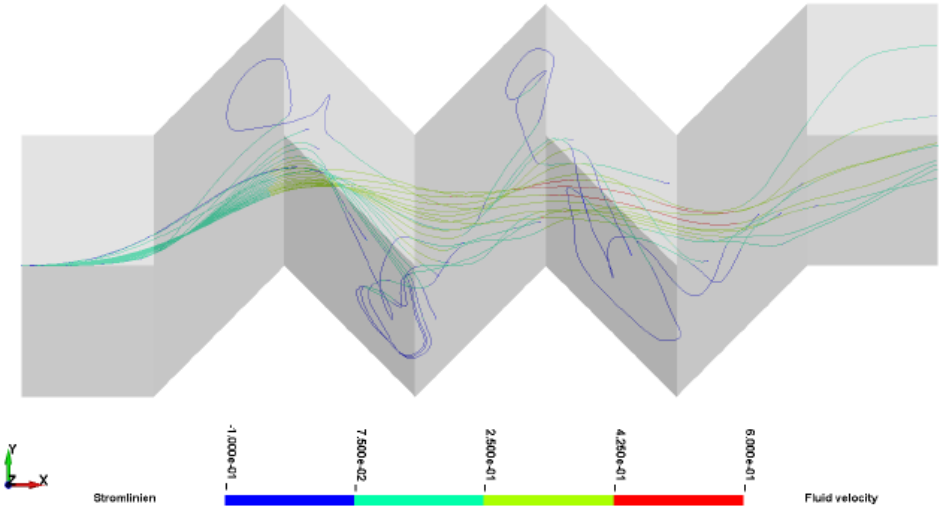

Fig.16: Streamlines for channel K3 in plan view [7].

6 Summary

In summary, with the exception of K1, the flow with folded cores can be reproduced very well in this work. However, it must be considered that strong convergence problems and implausible results are associated with conventional meshing. After switching to the meshing methodology developed in this work consisting of a fine resolution core flow mesh and a coarser mesh in the wall region, reasonable results could be obtained in acceptable simulation times. Validation of the numerical results using comparative simulations with OpenFoam and experimental data from the water channel was successfully performed. Thus, it could be shown that in principle a simulation of the flow is possible, but it is very much dependent on the geometry at hand and the boundary conditions of the flow. A more detailed examination of the individual influencing factors is the subject of future research work.

7 Literature

[1] Klett Y. Auslegung multifunktionaler isometrischer Faltstrukturen für den technischen Einsatz. 1st ed. München: Verl. Dr. Hut; 2013.
[2] Muhs F. Entwicklung eines numerischen Tools zur FE-basierten Auslegung und Optimierung von Faltkernen. 1st ed. München: Dr. Hut; 2021.
[3] Bohl W, Elmendorf W. Technische Strömungslehre: Stoffeigenschaften von Flüssigkeiten und Gasen, Hydrostatik, Aerostatik, inkompressible Strömungen, kompressible Strömungen, Strömungsmesstechnik. 15th ed. Würzburg: Vogel Buchverlag; 2014.
[4] Oertel H. Prandtl - Führer durch die Strömungslehre. Wiesbaden: Springer Fachmedien Wiesbaden; 2012.
[5] Gessner FB, Jones JB. On some aspects of fully-developed turbulent flow in rectangular channels. J. Fluid Mech. 1965;23(4):689–713.
[6] Idelčik IE. Handbook of hydraulic resistance. 3rd ed. Mumbai: Jaico Publ. House; 2005.
[7] Walter R. Numerische Untersuchung der Durchströmung von Faltkernen mit LS-Dyna. Masterarbeit. Stuttgart; 2021.
[8] Konrad P. Numerische Untersuchung der Durchströmung von Faltkernen. Diplomarbeit. Stuttgart; 2017.
[9] Wilcox DC. Turbulence modeling for CFD. La Cañada, California: DCW Industries; 2006.
[10] Roache PJ. Verification and validation in computational science and engineering. Albuquerque, NM: Hermosa; 1998.
[11] Gottschalk N. Analyse der Durchströmung von Faltkernstrukturen in einem Wasserkanal. Studienarbeit. Stuttgart; 2015.
[12] Schwarze R. CFD-Modellierung: Grundlagen und Anwendungen bei Strömungsprozessen. Berlin: Springer Vieweg; 2013.
[13] Holmen V. Methods for Vortex Identification. In: Mathematics.